CR-177908

FINAL REPORT

entitled

A New Methodology of Determining Directional Albedo Models from Nimbus 7 ERB Scanning Radiometer Measurements

by

Dr. Frederick B. House
HOUSELINE, INC.
2 Crest Lane
Swarthmore, PA 19081

prepared for

Dr. H. Lee Kyle, Code 910.2
Building 22, Room 372
Goddard Space Flight Center
National Aeronautics and Space Administration
Greenbelt, MD 20771

under

Purchase Order No. S-30544-D

August 1986

FOREWORD

This report is submitted to the Goddard Space Flight Center, National Aeronautics and Space Administration as a deliverable item pertaining to Purchase Order No. S-30544-D, dated 9-12-84 and amended 2-26-86. The scope of work concerns a review of the Nimbus 7 Earth Radiation Budget data set and to point out its strong and weak points. In view of the timing of this report relative to the processing schedule of Nimbus 7 ERB observations, emphasis is placed on a new methodology of interpreting the scanning radiometer data to develop directional albedo models. These findings enhance the value of the Nimbus 7 ERB data set and can be applied to the interpretation of both the scanning and non-scanning radiometric observations.

TABLE OF CONTENTS

A New Methodology of Determing Directional Albedo Functions from Nimbus 7 ERB Scanning Radiometer Measurements

1. Introduction

The Nimbus 7 ERB data set comprises observations by three separate instrument groups: the solar monitoring radiometers, the bi-axial scanning radiometers, and the non-scanning wide-field-of-view (WFOV) radiometers. The scanning radiometers have provided an excellent set of observations for a 19-month period following launch, and the non-scanning radiometers have monitored the solar irradiance and the radiant exitance of the earth until this year -- a period of more than 7 years of continuous observations.

The strengths of the data set are the excellent coverage of the bi-axial scanning radiometers and the long-term history of observations by the non-scanning instruments. At the time of this writing, the instrument performance of the WFOV radiometers is well understood, and the procedures for adjusting the instrument calibrations using the "Global CAT" methodology rests on a firm footing and has stood the test of time by many investigators. This was evident by the presentations of many papers at the 6th Radiation Conference in Williamsburg, VA which incorporated Nimbus 7 observations in their studies, and the WFOV measurements in particular.

However, there appears to be inherent value in the WFOV observations that is not fully realized with the format of the current presentation of results in the MATRIX archive. The problem rests with the repeat cycle of observations which is about 6 days for Nimbus 7's orbit. It takes 6 days, perhaps longer, to fill most of the bins so that a grid for

mapping the observations is complete. The weather systems have evolved during this time, and a map represents some composite space-time variation during the period of observations.

The suggestion here is to use Kalman filtering procedures to estimate the observational field on a daily basis. Such a procedure is a sophisticated interpolating technique in both time (forward and backward) and space. The observational field is portrayed by a set of continuous functions such as a Fourier series which is fit in an optimal sense to a finite set of observations. The coefficients of these functions are the determined quantity, and their values vary in time. Such a mapping procedure has been successfully applied to Nimbus 7 LIMS data processing, and to the mapping of NOAA scanning radiometer observations. Reasonably short data gaps are effectively filled by the Kalman filter procedures. Even a map for a missing day of data is estimated from observations from the preceeding and following days of data. Implementation of such a procedure would further enhance the usefulness of the ERB data set for scientific investigations.

The remaining portion of this report concerns a new method of determing directional albedo models from the scanner observations of reflected limb radiace using the principle of reciprocity. The unique feature of this methodology is that the directional albedo function is determined from observations of the same target area at a constant zenith angle of the sun. Thus, the restrictions of sampling from the Nimbus 7 orbit are relaxed, and directional albedo models may be determined from observations of any single target area of the world.

2. Theoretical Approach

Nimbus 7 ERB observations have limitations in their sampling of target areas as a function of solar zenith angle owing to measurements from a local noon, sun synchronous orbit. Overhead sun positions (small zenith angles) occur at tropical latitudes only, and lower sun positions (larger zenith angles) at mid-latitude and polar regions. Taylor and Stowe (1984) have studied the variation of albedo with solar zenith angle $a(\theta_0)$ by selecting similar targets at different latitudes, and then combining the observed albedos from these targets to form the directional albedo function. This approach implicity assumes that the physical properties of the radiometric surfaces and the atmospheric conditions are the same at different latitudes and changing seasons. The uncertainty of this approach is difficult to assess.

The properties of the directional albedo function may be inferred from observations of reflected radiances above a target area by applying the principle of reciprocity. The scanning radiometer on the ERB instrument observes reflected radiances $L_{sw}(\theta_0;\theta_e,\phi)$ for satellite view angles θ_e, azimuth angles ϕ with respect to the principal plane, and with a nearly constant solar zenith angle θ_0. Nimbus 7's orbit naturally constrains sampling at different θ_0 for a given latitude and time interval. However, the directional albedo function $\delta(\theta_0) = a(\theta_0)/a(0)$ may be approximated as a power of the direction cosine of the sun, $\delta(\theta_0) = \mu_0^p$, if reciprocity is assumed. The value of p is determined from the slope of a modified Minnaert plot of $\log(L_{sw}(\theta_0;\theta_e))$ against $\log(\mu)$ where $L_{sw}(\theta_0;\theta_e)$ are observed limb radiances after integration in azimuth ϕ, and μ is the

direction cosine of the satellite view angle, $\mu = \cos(\theta_e)$. This straightforward procedure of interpreting Nimbus 7 ERB observations seems to have been overlooked in the past, or not explored to its fullest extent. Its development follows below.

The bi-directional reflectance of a target area is defined as

$$R(\mu_0;\mu,\phi) = \pi \, L_{sw}(\theta_0;\theta_e,\phi) / \mu_0 E_0 \qquad (1)$$

which is the ratio of the actual reflection function to the reflection function of an ideal white (Lambert) surface. $\mu_0 E_0$ is the incident solar irradiance per unit surface area. In the reciprocity principle, the bi-directional reflectance may be reciprocated and is symetric. That is,

$$R(\mu_0;\mu,\phi) = R(\mu;\mu_0,-\phi) = R(\mu;\mu_0,\phi) \; . \qquad (2)$$

The first equal sign expresses the reciprocity principle, and the second equal sign states the symetry assumption. See van de Hulst (1980). For each (μ,ϕ) coordinate pair, there is a corresponding (μ_0,ϕ) pair. Thus, $R(\mu_0;\mu) = R(\mu;\mu_0)$ after integrating in azimuth to eliminate the strong forward scattering properties of bi-directional reflectance. If the magnitude of the flux from the sun arriving at the earth per unit area is π, then

$$L_{sw}(\theta_0;\theta_e) = \mu \, R(\mu_0;\mu) \quad \text{and} \quad L_{sw}(\theta_e;\theta_0) = \mu_0 \, R(\mu;\mu_0) \qquad (3)$$

using the definition in (1).

Minnaert (1941; see also Minnaert, 1961) has suggested an empirical relationship for interpreting photometric data from planets. This relationship is

$$L_{sw}(\theta_0;\theta_e,\phi)\,\mu = \text{const.}\,(\mu\mu_0)^k \qquad (4)$$

which obeys the reciprocity principle. This expression states that the radiance is described by the direction cosines and two constants. The plots of $\log(L\mu)$ against $\log(\mu\mu_0)$ from which the constant k is the slope are known as "Minnaert plots" (van de Hulst, 1980).

The procedure herein employs a modified form of the Minnaert plot. From (4), the limb radiance may be expressed as

$$L_{sw}(\theta_0;\theta_e) = \mu_0^k\, L_{sw}(0;0)\ \mu^p \qquad (5)$$

where the exponent $p = k - 1$. $L_{sw}(0;0)$ is the radiance for a zenith sun and a zenith view from the satellite. A plot of $\log(L_{sw})$ against $\log(\mu)$ from which the constant p may be read as a slope is the modified Minnaert plot. It will be shown below that the constant p is the exponent of the direction cosine of the directional albedo function.

Continuing with this line of reasoning, the reflected exitance $M_{sw}(\theta_0)$, the albedo $a(\theta_0) = M_{sw}(\theta_0)/\mu_0 E_0$, and the directional albedo function $\delta(\theta_0)$ are expressed in terms of equation (5). The reflected exitance as a function of solar zenith angle becomes

$$M_{SW}(\theta_0) = 2\pi \int_0^{\pi/2} L_{SW}(\theta_0;\theta_e)\, \mu \sin(\theta_e)\, d\theta_e$$

$$= 2\pi\, L_{SW}(0;0)\, \mu_0{}^K \int_0^{\pi/2} \mu^K \sin(\theta_e)\, d\theta_e \quad . \qquad (6)$$

The albedo expressed as a function of solar zenith angle is

$$a(\theta_0) = [2\pi\, L_{SW}(0;0)\, \mu_0{}^P \int_0^{\pi/2} \mu^K \sin(\theta_e)\, d\theta_e\,] / E_0 \quad . \qquad (7)$$

Note that the exponent p of the direction cosine μ_0 is the same constant as the slope of the modified Minnaert plot using (5). Finally, the directional albedo function is simply

$$\delta(\theta_0) = \mu_0{}^P \qquad (8)$$

since all the other terms cancel on division of $a(\theta_0)$ by $a(0)$ using (7).

The reciprocity principle holds if the surface properties of the target are the same. In this approach, the reflecting properites of just one surface determine the directional albedo function. One avoids the assumptions of common surfaces properties of targets at different latitudes and constant atmospheric conditions. Simply stated, if the observed limb radiances of a target $L_{SW}(\theta_e)$ are constant with θ_e, the reflecting surface is flat and obeys Lambert's Law. If the radiances are limb brightened, the directional albedo increases with θ_0. Conversely, if the radiances are limb darkened, the directional albedo decreases with θ_0. As a rule, the radiances are usually limb brightened. However, there are

exceptions for high sun positions and the southern hemisphere during the summer season.

The value of the constant p describes the reflecting properties of a target and may be used as a tag for comparing directional albedos of different target areas, and changing seasonal conditions. This exponent varies over a range from about +0.2 to -0.8 in magnitude, and Figure 1 illustrates the interpretation of different p values. If $p > 0$, the target is limb darkened, and for negative values, $p < 0$, the target is limb brightened. In the special case where $p = 0$, the target reflects as a Lambert surface, and radiances are constant (isotropic) for different satellite view angles. When examining the Figures presented in Section 4 of the results, the zero line on a graph may be used to delineate limb brightened targets from those that are limb darkened. Limb brightening implies increasing albedo with solar angle (-p values), and limb darkening denotes decreasing albedo with solar angle (+p values).

3. Data Processing Procedures

The ERB scanning radiometers on Nimbus 7 satellite observed reflected radiances from the earth during the 19 months of operation from November 1978 through June 1980. Usually the instrument was operated on a duty cycle of 3 days on and 1 day off. It is conventient to process observations for one 3-day period, or groups of 3-day periods, and to select those periods when the scan mode optimized the angular coverage of observations.

An estimate of reflected radiance from a target area for a particular coordinate direction (θ_e,ϕ) is determined from the time average of all radiances falling in a bin defined by angular ranges $\Delta\theta_e$ and $\Delta\phi$, centered at (θ_e,ϕ). This study employed a 64-bin division of the hemisphere above the target area including 8 bins of view angle with $\Delta\theta_e = 10°$ from 5° to 85°, and 8 bins of azimuth with an interval of $\Delta\phi = 45°$ each. The azimuth bins were centered on the forward and backward scattering directions with respect to the principal plane. The zenith angle of the sun θ_0 is also an average value varying during the period of observation, the latitude range of the target (10°), and the local time of observation during satellite fly-bys. The computer code compiles observations for every 10° latitude interval from 85°N to 85°S. The selection of a 10° latitude zone is a compromise between averaging time, changing declination of the sun and adequate sampling of target areas.

The results presented in Secion 4 emphasize seasonal and monthly groupings of the observations (Table 1). Each seasonal period comprises 21 days of measurements where the selected dates include the vernal equinox (March 21), the atumnal equinox (September 22), the cold of winter (February 1) and the heat of summer (August 1). The opposite seasons of fall, spring, summer and winter, respectively, occur in the southern hemisphere. Each latitude zone has a sampling population of about 240,000 scanner observations during a 21-day seasonal period.

Eight 3-day periods were chosen with dates to compliment the four seasonal times shown in Table 1. Unfortunately, the month of October is the only missing period in the list because the compiled file was not useable for this study. However, the fall/spring seasonal observations for the period centered at day 265 of the year does include early October measurements in 1979. When compiling radiances for each latitude zone, all measurements for a 3-day period were processed together as one group.

In the case of the four seasonal periods, observations of radiance are averaged for the entire sample of 240,000 observations, and are then subdivided in to estimates of radiance for selected geopraphical areas including land, ocean, dessert, tundra, and land/ocean mixed (coastal regions). Further subdivisions at each latitude include mountains and plains for land regions; Pacific, Atlantic, Indian and Arctic for ocean regions; all desert areas for each latitude zone; and, the continent of Antarctica is considered a continent in the land/tundra classification. The directional albedo function may be intercompared among each of these geographical regions, and among latitudes where each classification occurs.

Table 1

Monthly and Seasonal Observation Periods
Employed in this Study

*Mid Date of Period	Day of Year	Season NH/SH	21-day Period	3-day Period
1/8/79	8			X
2/1/80	32	Win/Sum	X	
3/5/79	64			X
3/21/80	80	Spr/Fall	X	
4/28/79	118			X
5/24/79	144			X
6/17/79	168			X
7/11/79	192			X
8/1/79	213	Sum/Win	X	
9/22/78	265	Fall/Spr	X	
11/21/78	325			X
12/7/78	341			X

*The periods are not consecutive in time, but may occur one year later.

4. Analysis of Results.

The methodology of data analysis developed in the theoretical approach of Section 2 was applied to the Nimbus 7 ERB scanning observations of Table 1 in the manner outlined in Section 3. Four seasons were explored in detail for 10 classifications of geography and 17 different latitudes each. Twelve monthly periods of radiances were processed for 17 different latitudes. Then these results were combined to form generalized groups of directional albedo models. The possible combinations grow rapidly, and about 1,000 individual data points were analyzed before the study was complete.

The discussion of the results below summarizes the essential features of the directional albedo variations shown in the 26 Figures attached to this report. Only brief comments concerning the graphs are mentioned below -- it is hoped that the reader will examine the plots of data and draw his or her own conclusions. Perhaps a road map outlining the grouping of these results will aid the reader in directing ones attention to particular areas of interest.

Section 4.1 Figures 2 - 7 => typical seasonal examples of the Theoretical Approach of Section 2 including figures of exponent p variations, modified Minnaert plots, and actual fits to observed limb radiances.

Section 4.2 Figures 8 - 13 => interesting seasonal variations of directional albedo functions for selected target classifications including mountains, deserts and the Indian Ocean.

Section 4.3 Figures 14 - 16 => monthly and annual variations of the directional albedo function for combined regions at different latitudes.

Section 4.4 Figures 17 - 21 => generalized seasonal and annual variations of the directional albedo functions for selected target classifications.

Section 4.5 Figures 22 - 26 => comparison of study results with directional albedo models used in the ERBE data processing system (release 3).

4.1 Seasonal Variations - Modified Minnaert Plots.

Figures 2 - 4 illustrate results for the spring southern hemisphere (SH) and fall northern hemisphere (NH) seasons where all data are grouped together. In Figure 2, the variation of the exponent p in equation (6) ranges from -0.4 in polar regions of the SH to 0.0 in the tropics to -0.5 in the polar regions of the NH. If one were employing this model to process scanner data, a different power of p would be used at each latitude to interpret the diurnal variation of albedo with solar angle of the sun.

The results shown in Figure 3 and Figure 4 illustrate typical regression fits to observed limb radiances using the approach of a modified Minnaert plot. Figure 3 shows examples of three plots for latitudes in the SH similar to other plots used to generate the exponents in Figure 2. The trend lines were fit to the observations using the method of least squares where the slope of the line defines the exponent p. The standard estimates of the linear regressions are ±0.011 for 70°S, ±0.009 for 40°S, and ±0.017 for 10°S. Note the linearity of the observed limb radiances even though the

scenes are heteorogeneous including observations from clouds, land areas, ocean areas, deserts, etc. This result confirms the assumption that the reciprocity principle may be applied to heteorogeneous scenes as well as homogeneous, pure scenes.

Figure 4 shows the acutal fit to the observed limb radiances corresponding to the regression lines in Figure 3 of the Minnaert plots. The computed rms differences between the observed radiances and their estimates are ±2.6 W/(m^2-sr) at 70°S, ±2.1 W/(m^2-sr) at 40°S, and ±3.4 W/(m^2-sr) at 10°S. These examples are representative of the results of this study.

Figures 5 - 7 present a similar grouping of graphs for the summer SH and winter NH seasons. Figure 5 illustrates the variation of the exponent p with latitude where it is noted that $p \approx 0$ for all latitudes in the SH during summer. This implies that the surface obeys the Lambert Law for all prictical purposes, and that the directional albedo function is constant and ≈ 1. During other times of year, the exponent is quite negative in value as for spring in Figure 2. In the NH, the exponent decreases rapidly from 0 to a value of -0.7 at latitude 60°N.

Figures 6 and 7 show Minnaert plots and radiance estimates for selected latitudes in the NH winter. Note that the slopes of the regression lines are more negative compared to those of Figure 3 for SH spring. The rms differences are ±4.2 W/(m^2-sr) for 60°N, ±5.1 W/(m^2-sr) for 40°N, and ±0.7 W/(m^2-sr) for 10°N. Some of the rms difference is due to observational

bias when compiling average radiances from a finite number of satellite observations.

4.2 Seasonal Variations of Selected Regions.

A selection of interesting seasonal variations is presented in Figures 8 - 13 where the results portray some of the observations for specific target areas. Figure 9 presents limb radiance observations for mountain regions in the SH summer at latitudes 10°S and 40°S. The observed radiances exhibit limb darkening at 10°S, and the corresponding exponent value for these observations is $p = +0.13$ in magnitude. Likewise, the magnitudes of the radiances of about 180 $W/(m^2\text{-}sr)$ are as large as any observed in the rest of the world. The observations are probably associated with convective activity across central South America and Africa. In contrast, the radiances at 40°S exhibit typical limb brightening where the exponent value is -0.06 in magnitude.

The exponent values for desert areas of the world are shown in Figure 10 for latitudes 20° to 40° during winter in the NH and summer in the SH. The values of p are negative during winter and positive during summer. However, the signs reverse six months later when the NH desserts have positive values and the SH deserts negative values. Also shown is the exponent of -0.03 for the continent of Antarctica (see square black symbol of Figure 10).

Figures 11 and 12 illustrate the variation of limb radiances for the desert regions of Figure 10. In the NH all radiance profiles are limb brightened (Figure 11) whereas all profiles in Figure 12 are limb darkened. The associated values of p vary from -0.27 to -0.06 in the NH, and +0.03 to +0.11 in the SH.

An interesting sequence of exponents is observed for the Indian Ocean region in Figure 13 between latitudes 20°N and 80°S. The values are about zero in magnitude for the entire SH, but decrease rapidly to -0.47 at 20°N. The NH oceans here are the Bay of Bengal east of India and the Arabian Sea. Obviously, the optical properties of the ocean and atmosphere in the NH are much different than those in the SH.

4.3 Monthly and Annual Variations of Combined Regions.

Figures 14 - 17 summarize observations of the exponent p for the twelve periods listed in Table 1. Figures 14 and 15 show the variation of p during the year for latitudes 60°, 40°, and 10° in the NH and SH, respectively. The values of p seem coupled principally to the changing declination of the sun where the exponent increases as winter approaches and decreases as summer approaches in both hemispheres. The seasonal ranges are largest at high latitudes ranging from about -0.1 to -0.8 from summer to winter. The corresponding ranges of exponent are about 0.0 to -0.4 at mid latitudes and 0.0 to -0.2 at tropical latitudes.

Suppose one were developing a generalized directional albedo model for a period of one year and for the entire world. Results show that the average annual exponent would be p = -0.2 in magnitude. Perhaps, the next level of model sophistication would be to consider the variation of exponent with latitude for the average of twelve monthly periods. Such results are shown in Figure 16 where the values range from -0.37 at 60°N to -0.05 in the tropics to -0.44 at 60°S. The magnitudes at polar latitudes are somewhat smaller than those at 60° latitude owing to the seasonal transition into polar night during winter and, perhaps, different reflecting properties of the surfac and atmosphere.

An interesting scatter plot of all exponent values for the entire year is presented in Figure 17 where the values are plotted as a function of the zenith angle of a noon sun. This angle would be defined as the absolute difference between the declination of the sun and the latitude of observation. Of course this angle changes continuously through the course of the year, and the exponent value in the directional albedo function would also change. The observations indicate that the earth reflects as a Lambert surface for zenigh angles less than 20°. Then the value of p decreases to a magnitude of about -0.7 for a noon sun angle of 80°. The scatter of points is least for a high sun position and tends to diverge for lower sun potions. Most of the scatter of values is associated with seasonal variations at sun angles greater than 45° where observed exponents decrease markedly during SH summer. A simple model of directional albedo may be developed by drawing an average curve through the scatter of points taken to be the annual mean variation, and then to account for the seasonal variations at

each sun angle. Such a procedure would be accurate to about ±0.1 of the observed value of the exponent.

4.4 Generalized Variations in Space and Time.

Figures 18 - 21 portray the variations of the exponent with season for different latitudes and target classifications. In Figure 18, the observations show the variation of exponent values in the NH as the scene changes the year. Exponent values are more negative in winter, least negative in the summer, and vary between the extremes during fall and spring. The seasonal range of variations is practically constant at the equator and is a maximum at high latitudes.

Desert regions of the earth generally have more uniform surface properties and fewer clouds compared to other areas of the world. Figure 19 shows the seasonal variation of exponent values for the desert classification. Here the scatter of points is small and the variation with season significant. For zenith angles of the noon sun less than 25°, deserts appear to be limb darkened which corresponds to their summer seasons. For high noon sun angles, $p \approx +0.1$ in magnitude. Values decrease from 0.0 to -0.2 for the spring and fall seasons, and continue to decrease to -0.3 during winter.

Similar plots are presented for the land classification in the NH (Figure 20), and for the ocean regions in the SH (Figure 21). It is interesting that the variation with sun angle of the exponent values is about the same

for each classification, but there is a slight offset difference at the ordinate. The values for the ocean areas are somewhat lower than those for the land regions which are, in turn, lower than those for the desert exponents. This suggests that the controlling factor in the diurnal variation of the reflecting properties is, not so much the underlying surface properties, but the atmosperic conditions varying throughout the year. In other words, the variation of the exponent is much greater with season (sun angle) than it is between different target classifications. This is an important result when constructing directional albedo models for data processing systems of earth radiation budget observations.

4.5 Comparisons with ERBE Directional Albedo Models.

As a final point of discussion, the results of this study are compared with the directional albedo models employed in the ERBE data processing system (release 3). The ERBE methology employs 12 models of which 5 are associated with clear skies (CLR) and ocean, land, snow, desert and land/ocean mixed surfaces; 3 partly cloudy (PC) models for ocean, land-desert-snow, and mixed surfaces; 3 mostly cloudy (MC) models for ocean, land-desert-snow, and mixed surfaces; and, 1 model for overcast (CLDY) cloud conditions. These models are derived from homogeneous surfaces as defined by a scene identification algorithm. The results of this study are for average scenes where CLR to CLDY conditions are mixed, together. One would anticipate that the average ERBE models for PC and MC scene types would compare favorably with the models of this study. However, the variations of the models herein are much greater for heteorogeneous targets

than are the variations in ERBE models for pure scene types. This is an unexpected result of the study.

The comparison of desert models is presented in Figure 22 where the directional albedo function in equation (8) is plotted as a function of the cosine of the solar zenith angle μ_0. Each ERBE desert model is identified by the black triangles and the cloud condition acronymn. The bounding range of models associated with this study are plotted as lines and identified with their associated value of exponent. For example, the desert models range seasonally for values $-0.3 \leq p \leq 0.1$ in magnitude as was shown previously in Figure 19. The comparison of the shape of the models is excellent. However, the results of this study suggest limb darkened models for summer seasons, and somewhat less variation in albedo for limb brightened models compared to the ERBE directional albedo.

Similar comparisons are presented in Figures 23 - 25 for land, ocean and land-ocean mixed models, respectively. When looking at these graphs, the models of this study indicate a much larger variation in the directionality of albedo as compared to the ERBE models. This is attributed to the seasonal variation mentioned earlier which seems to dominate the change in directional albedo models.

The comparison of snow models is shown in Figure 26 where the data from this study are associated with the geographical areas of the

Antarctic continent, and the northern latitudes of Asia and North America. Again, the study results show that the variations of directional albedo are greater than those for the ERBE models. This is also attributed to seasonal variations of atmospheric conditions.

5. Summary and Conclusions

Directional albedo models define the physical properties of reflection by describing the variation of albedo as a function of the solar zenith angle. The observations by the ERB scanning radiometers on Nimbus 7 satellite are particulary suited to examine the spatial and temporal variations of the earth albedo. However, the sampling of target areas as a function of solar zenith angle is naturally constrained by measurements from a local noon, sun sychronous orbit.

It is shown in the theoretical approach of Section 2 that the properties of the directional albedo function may be inferred from observations at a constant zenith angle by applying the principle of reciprocity. Thus, the restrictions of sampling radiances at different solar zenith angles from the Nimbus 7 orbit are relaxed. The directional albedo function is defined as an exponent p of the direction consine of incident solar radiation μ_0., that is, $\delta(\theta_0) = \mu_0{}^p$. The value of p is read from the slope of a modified Minnaert plot of the log of limb radiance against the log of the direction cosine of the satellite view angle.

Observations of limb radiance from Nimbus 7 satellite are assembled into four seasonal periods with 21 days of data each, and 8 additional monthly periods with 3 days each. Seasonal data were grouped into geographical regions including land, ocean, desert, tundra for 10° latitude zones from 80°N to 80°S. About 1,000 combinations of models are examined by analyzing the variation of the exponent p determined from the Minnaert plots.

The method of least squares is used to fit linear regression lines to the observations on the modified Minnaert plots. Typical standard estimates of the error range from ±0.01 to ±0.02, and the corresponding rms differences in the fit to the radiances are about ±2 W/(m^2-sr) to ±4 W/(m^2-sr), respectively. The results indicate that the principle of reciprocity may be applied to composite observations from heterogeneous scene groups.

In the results of Section 4, the variations of the exponent p are examined for monthly and seasonal changes in atmospheric conditions, and for different geographical groupings of the satellite observations. The results are presented in Figures 2 through 26 of the report. Values of p range from +0.15 for tropical mountains (a limb darkened scene), to negative exponents of -0.90 for winter at high latitudes)a strongly limb brightened scene). A value of p = 0 corresponds to a Lambert surface having no directionality in the albedo function.

Three important conclusions of the study are: (1) seasonal variations of atmospheric conditions dominate the variations in the directional albedo function; (2) the type of underlying surface has a second order effect compared to the seasonal changes in atmospheric conditions; and, (3) the overall variation of heterogeneous scene models from this study is significantly larger than those described by the ERBE models for pure scene types.

REFERENCES

Minnaert, M., Astrophys. J., 93, 403, 1941.

Minnaert, M., In "The Solar System" (G. P. Kuiper and B. M. Middlehurst, eds.), Vol. III, Planets and Satellites, p. 213, Univ. of Chicago Press, Chicago, Illinois, 1961.

Taylor, V. R. and L. L. Stowe, Reflectance characteristics of uniform earth and cloud surfaces derived from Nimbus-7 ERB, J. Geophys. Res., 89, D4, 4987-4996, 1984.

van de Hulst, H. C., Multiple light scattering - tables formulas, and applications, Vol. 2, Academic Press, New York, 614-617, 1980.

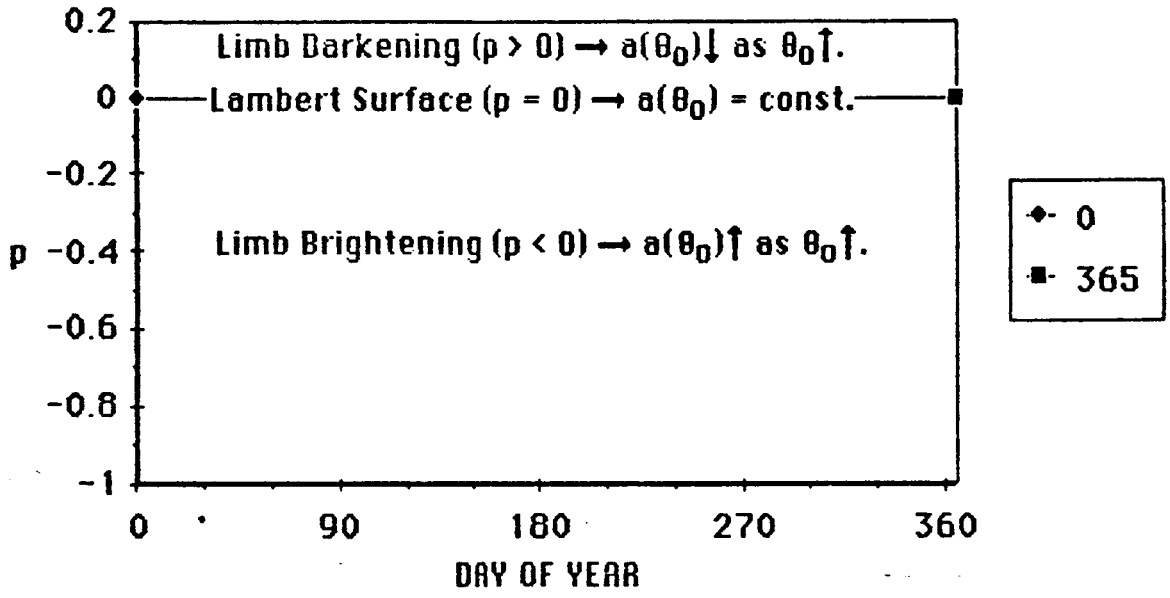

Fig. 1 Interpretation of the optical properties of the exponent p in the directional albedo function of equation (6).

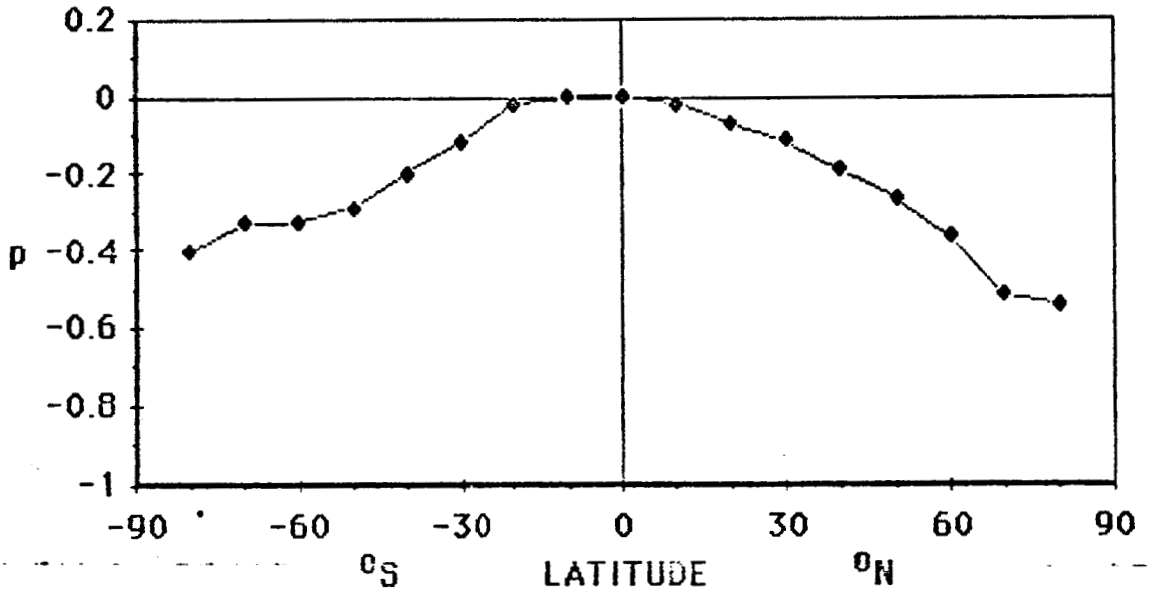

Fig. 2 Variation of the exponent p with latitude during the southern hemisphere (SH) spring and northern hemisphere (NH) fall seasons. These results are based on limb radiances determined from all observation.

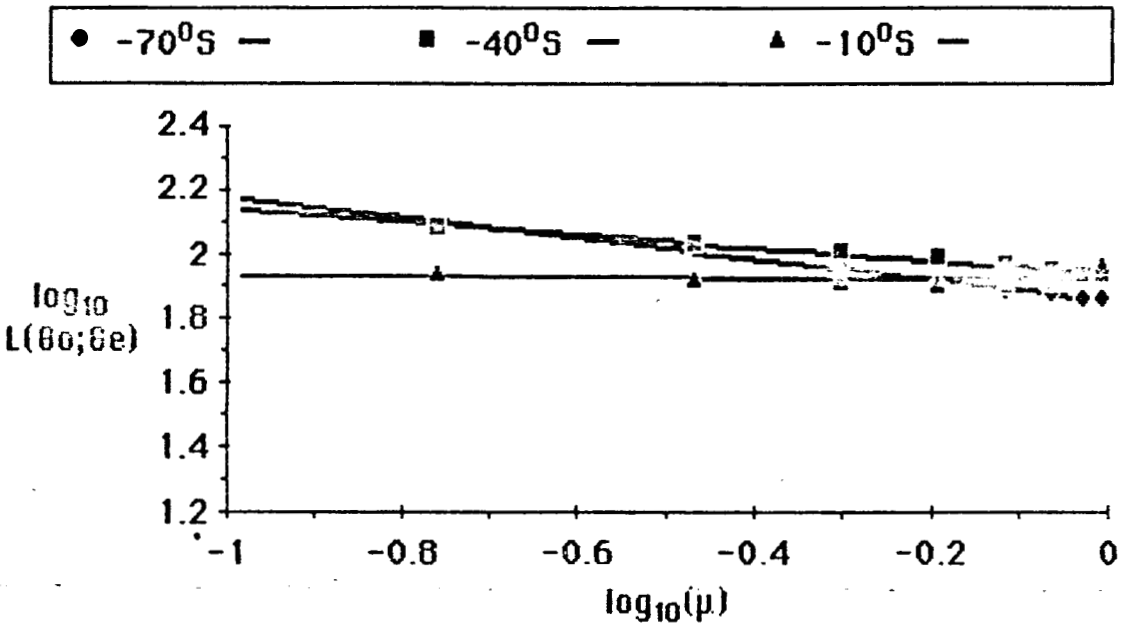

Fig. 3 Modified Minnaert plots of radiances at selected latitudes in the SH. The slopes of these regression lines are the exponent values p which are plotted in Figure 2.

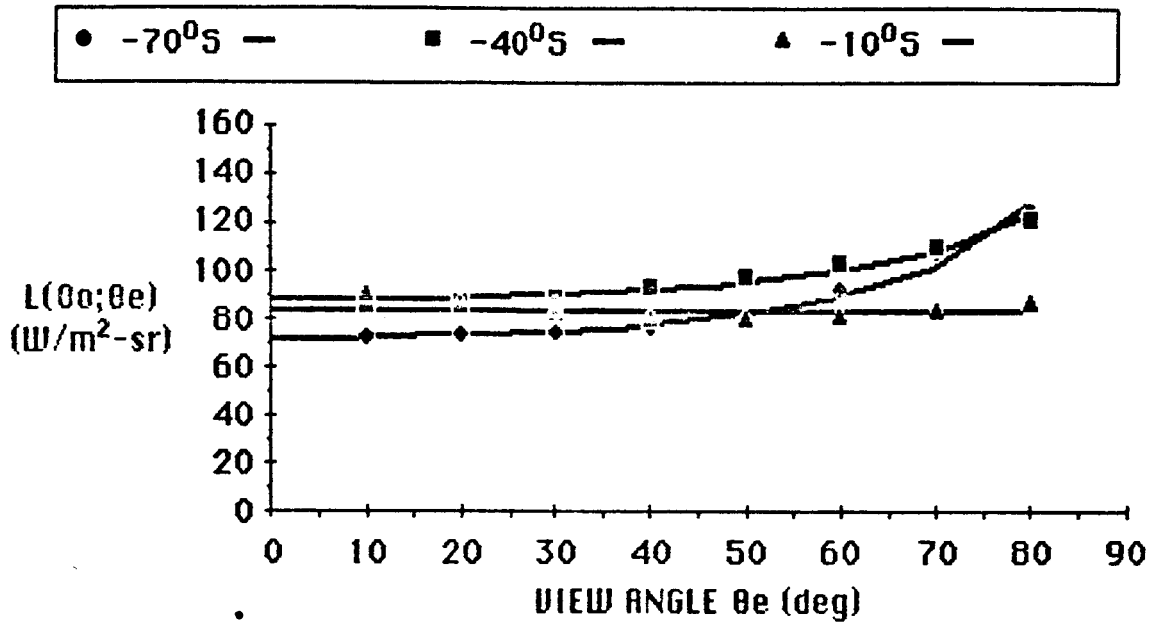

Fig. 4 Comparison of the actual fit to the observed limb radiances corresponding to the regression lines determined in Figure 3.

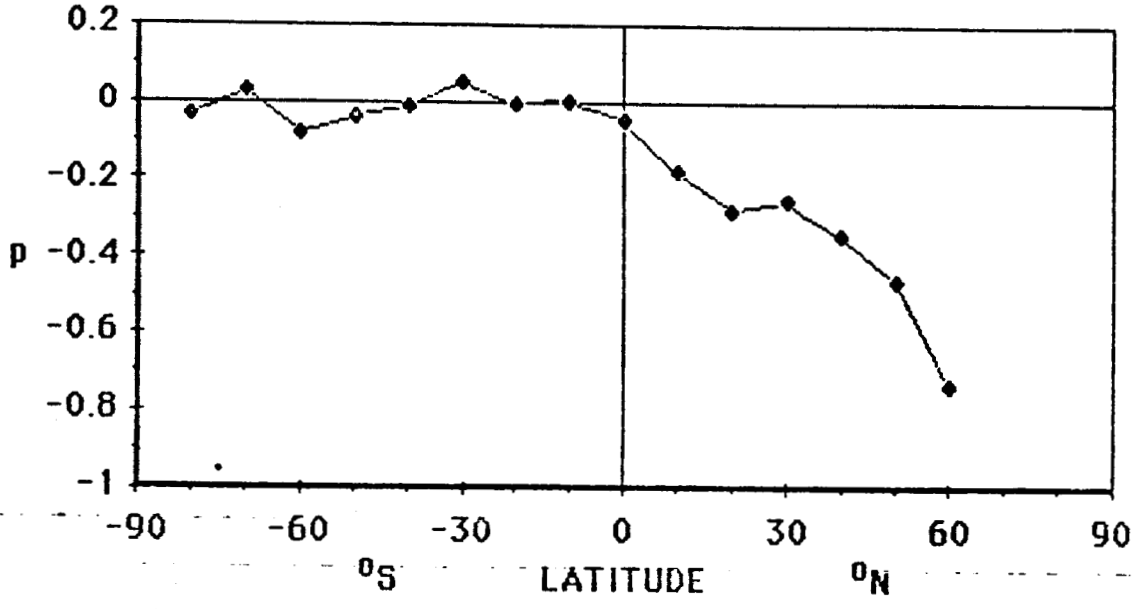

Fig. 5 Variation of the exponent p with latitude during the SH summer and NH winter seasons. These results are based on limb radiances determined from all observation.

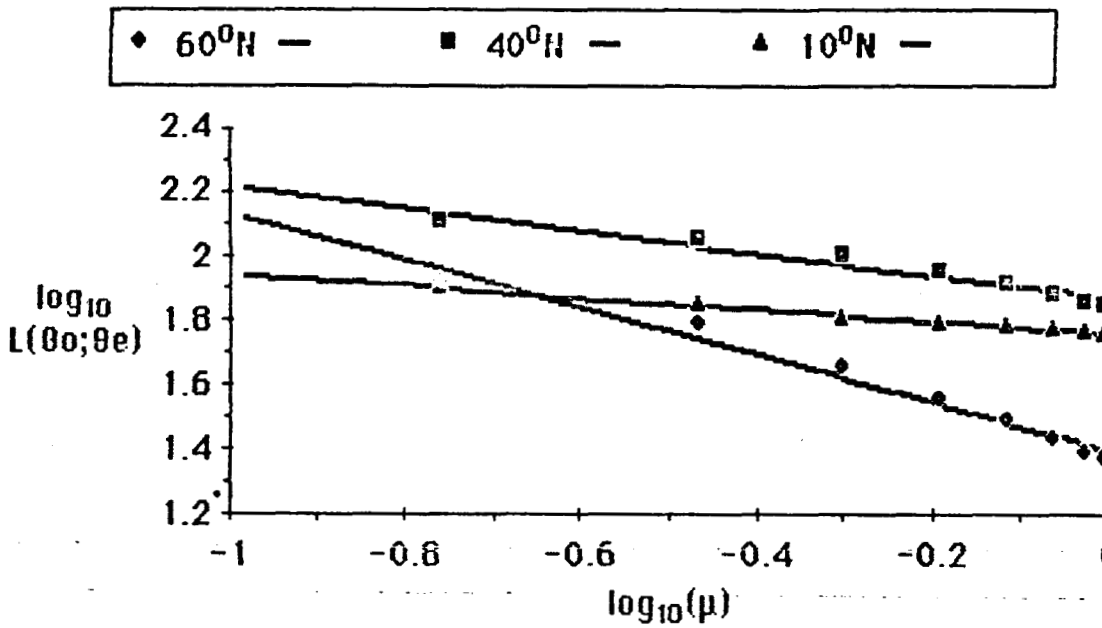

Fig. 6 Modified Minnaert plots of radiances at selected latitudes in the NH. The slopes of these regression lines are the exponent values p which are plotted in Figure 5.

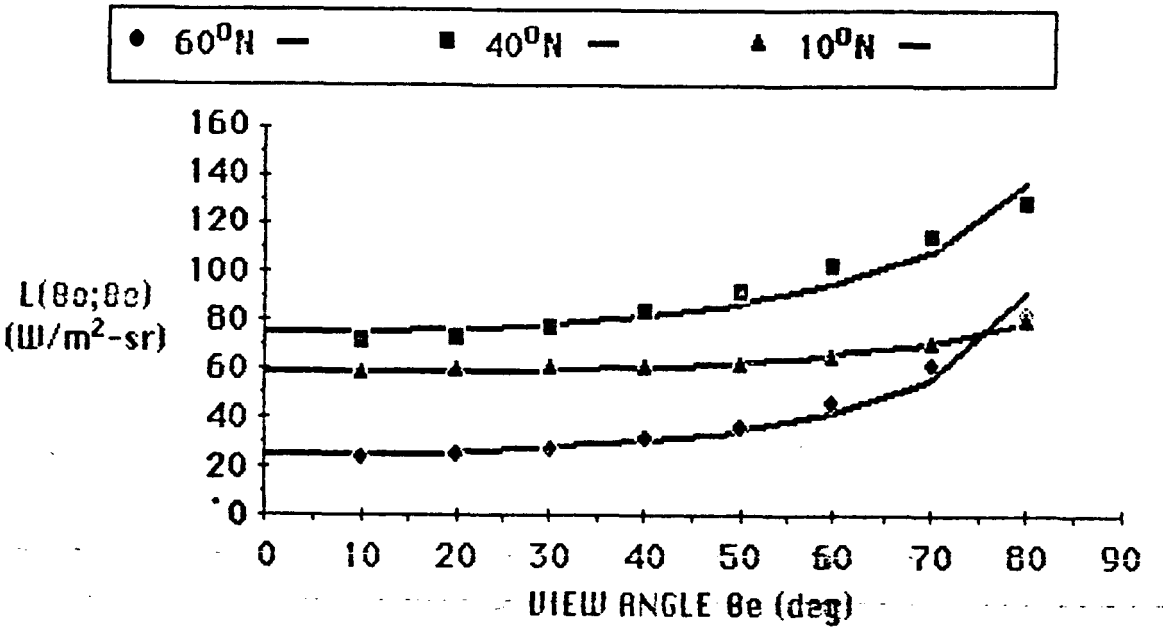

Fig. 7 Comparison of the actual fit to the observed limb radiances corresponding to the regression lines determined in Figure 6.

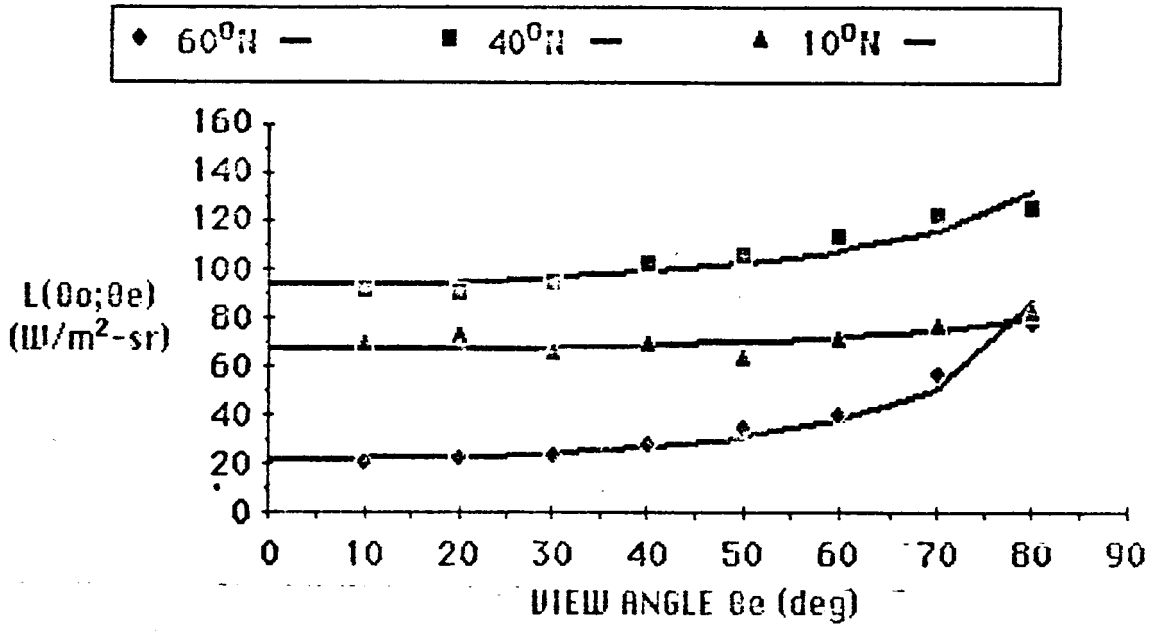

Fig. 8 Limb radiance observations for mountain regions at selected latitudes during the NH winter season. The curved lines show regression fits to the limb brightened radiances.

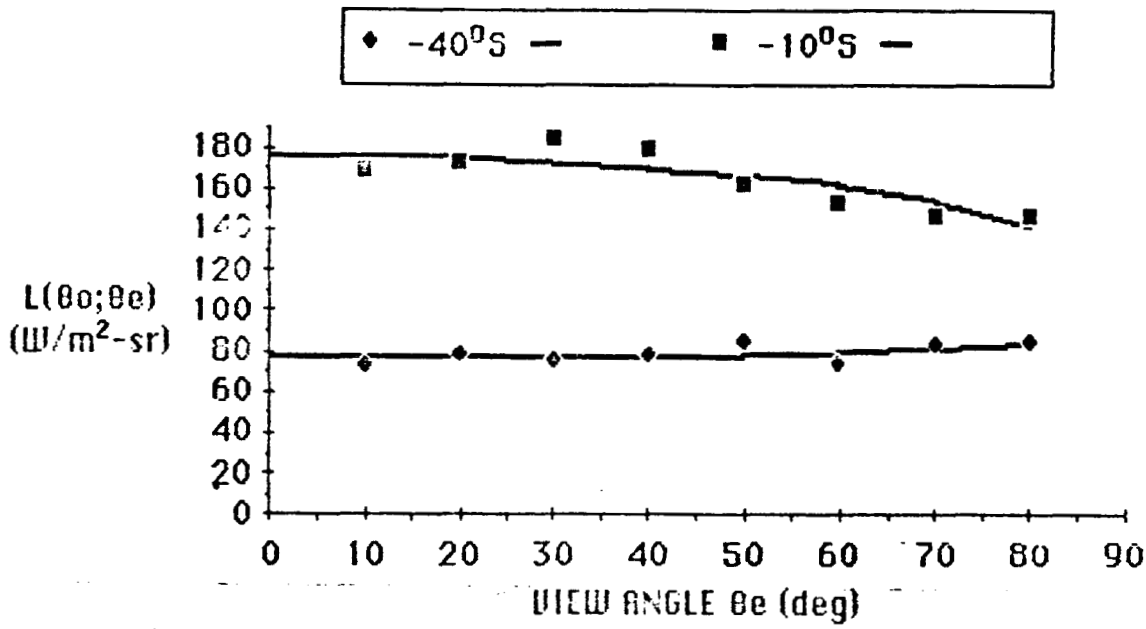

Fig. 9 Limb radiance observations for mountain regions at selected latitudes during the NSH summer season. The curved lines show regression fits to the observed radiances.

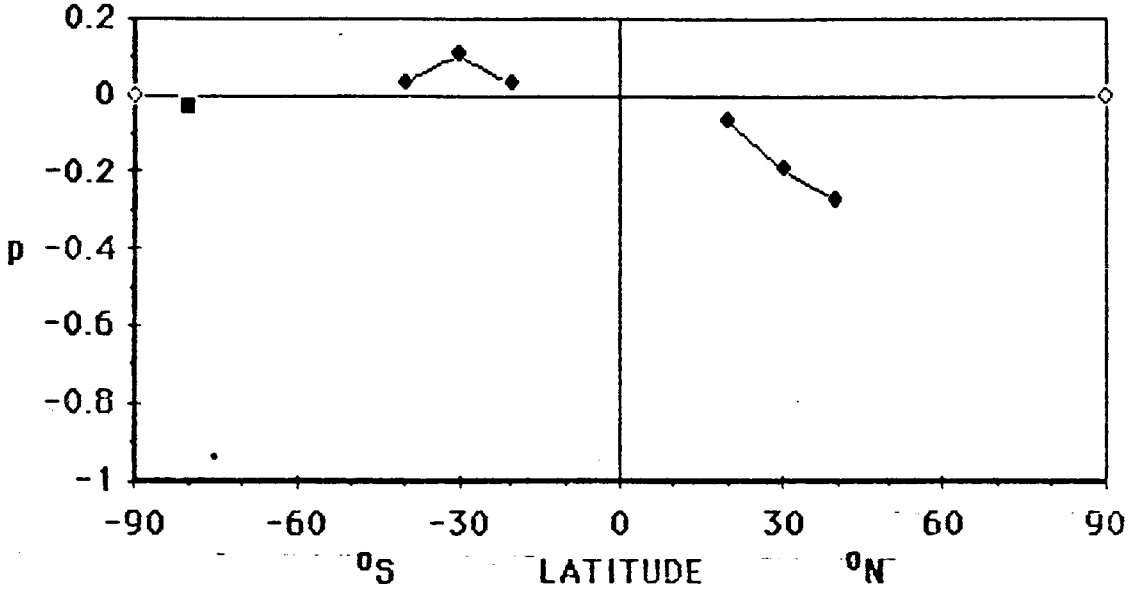

Fig. 10 Variation of the exponent p with latitude for desert regions of the world during the SH summer and NH winter seasons. The black square at -80°S is the exponent for Antarctica.

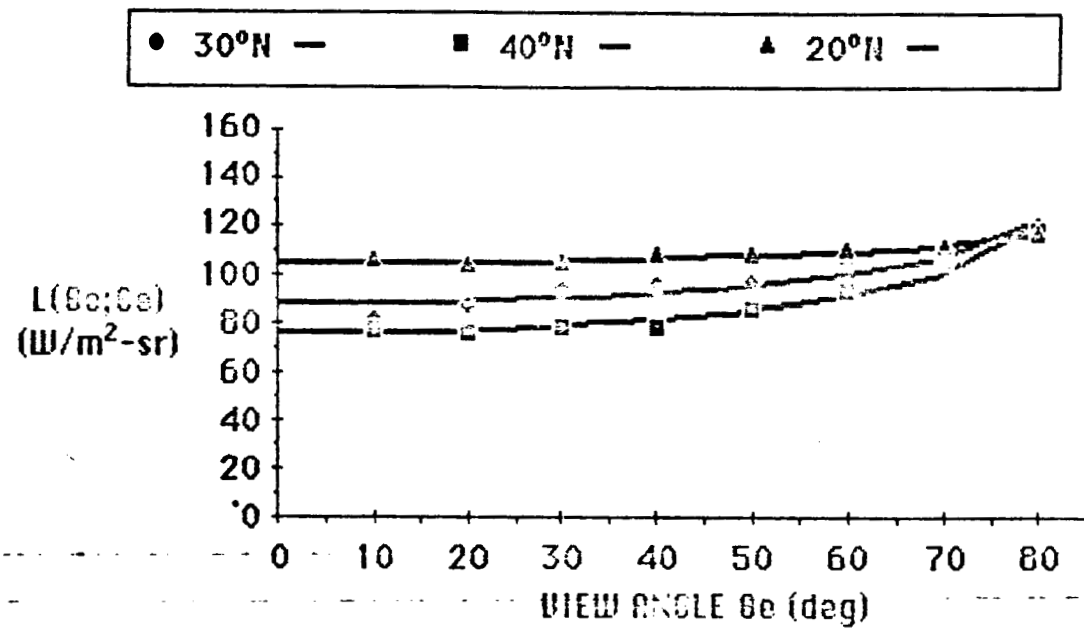

Fig. 11 Limb radiance observations for desert regions during the NH winter shown in Figure 10. The curved lines show regression fits to the observed radiances.

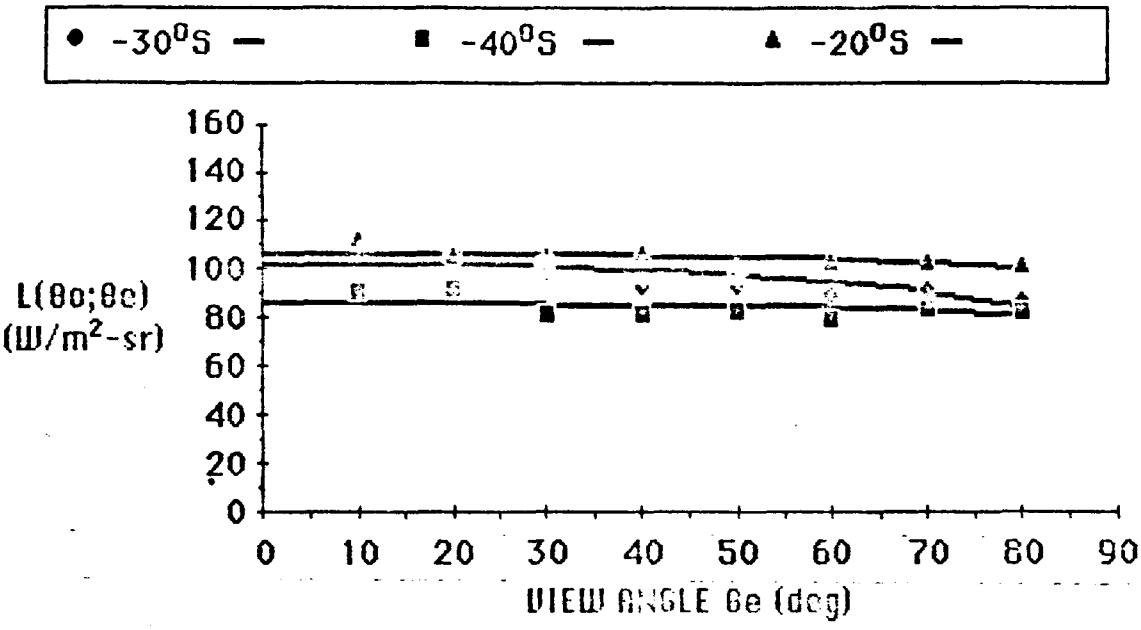

Fig. 12 Limb radiance observations for desert regions during the SH summer shown in Figure 10. The curved lines show regression fits to the limb darkened radiances.

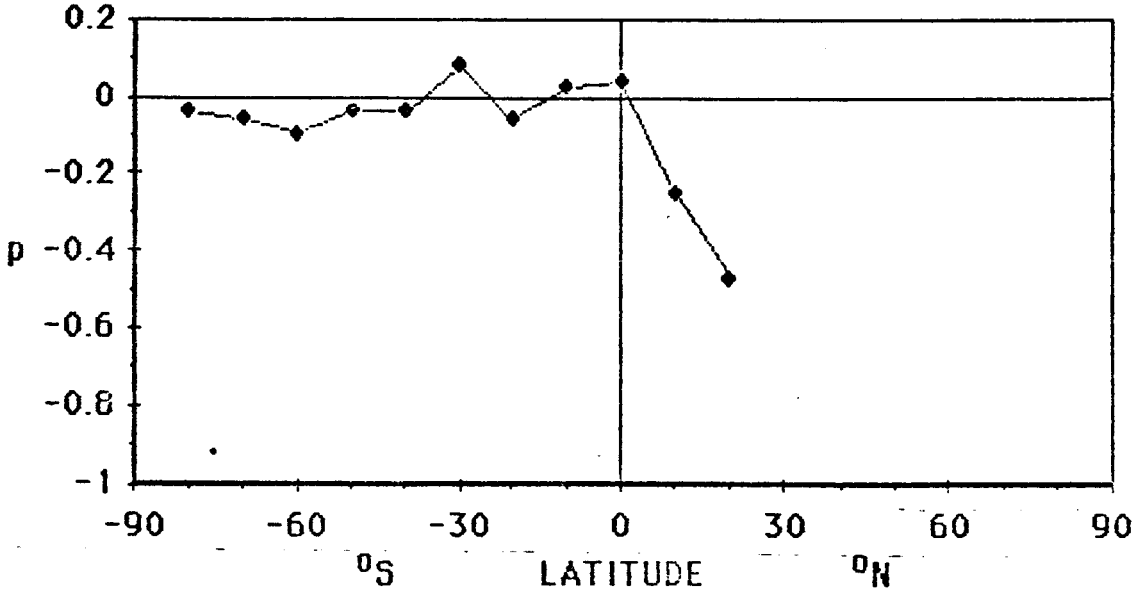

Fig. 13 Variation of the exponent p with latitude for the Indian Ocean region during the SH summer and NH winter seasons. Note the rapid decrease of the exponent in the NH over the Bay of Bengal and the Arabian Sea.

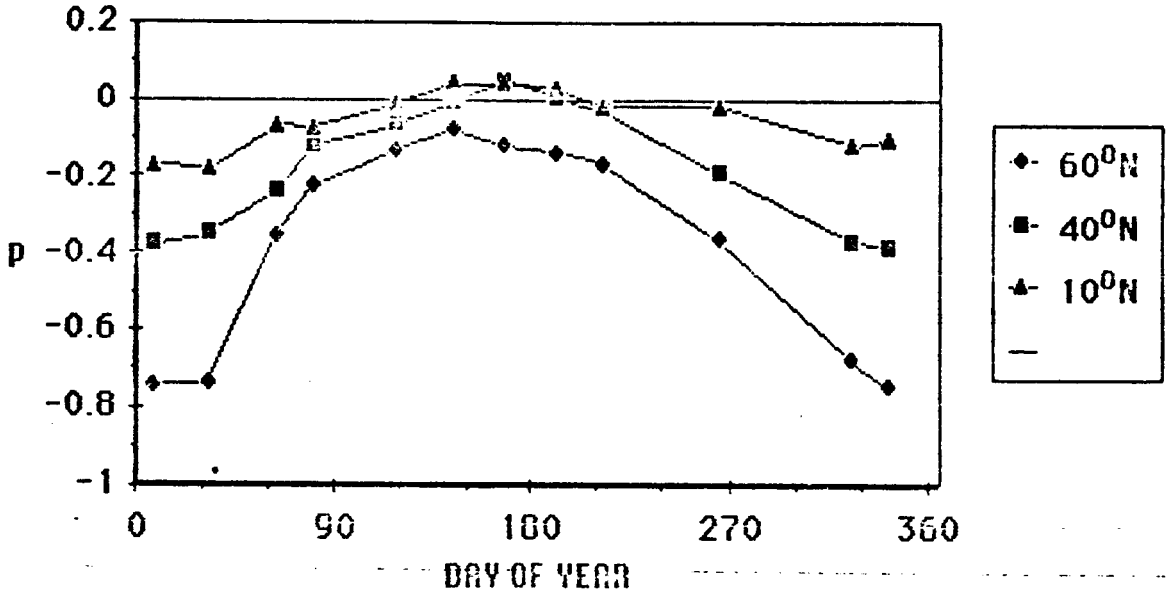

Fig. 14 Annual variation of the exponent p at selected latitudes of the NH.

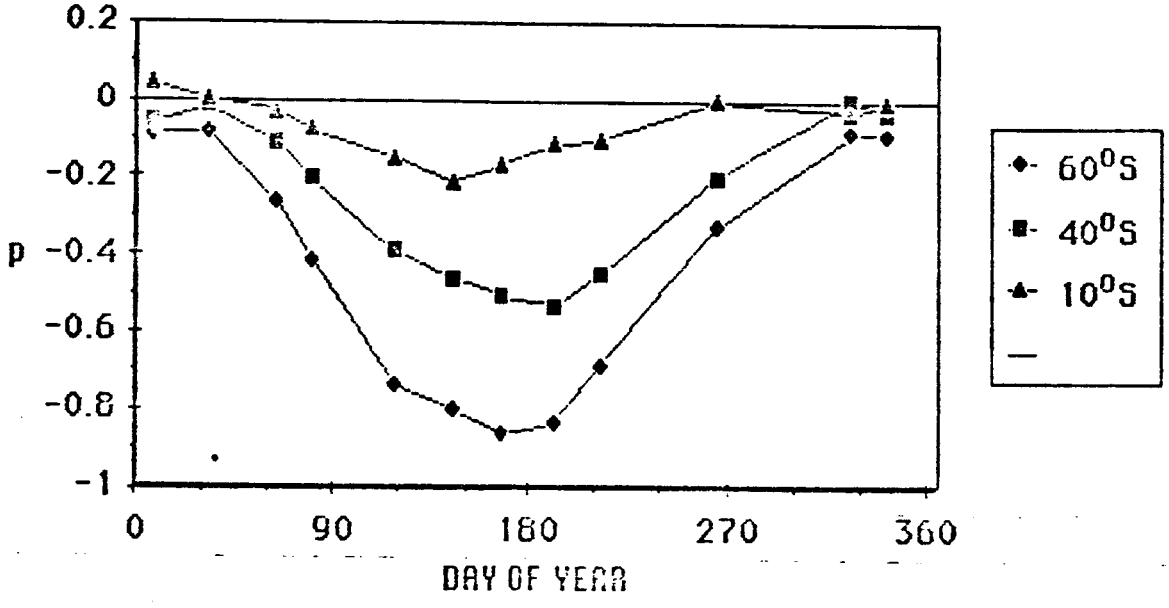

Fig. 15 Annual variation of the exponent p at selected latitudes of the SH.

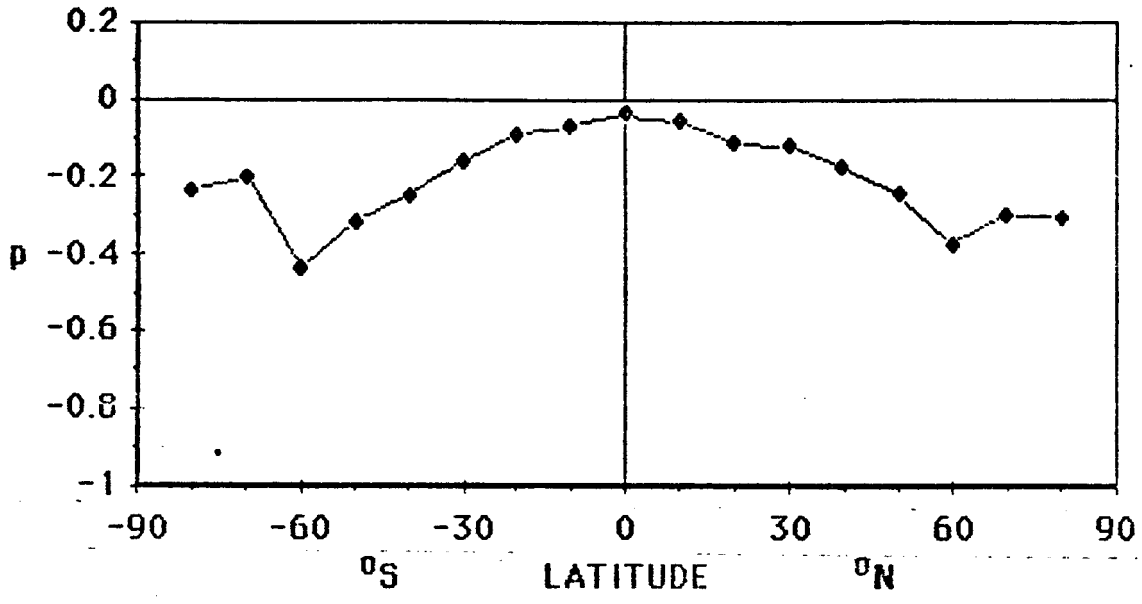

Fig. 16 Latitude variation of the annual average value of the exponent p. The average value of the exponent is -0.2 for the entire world.

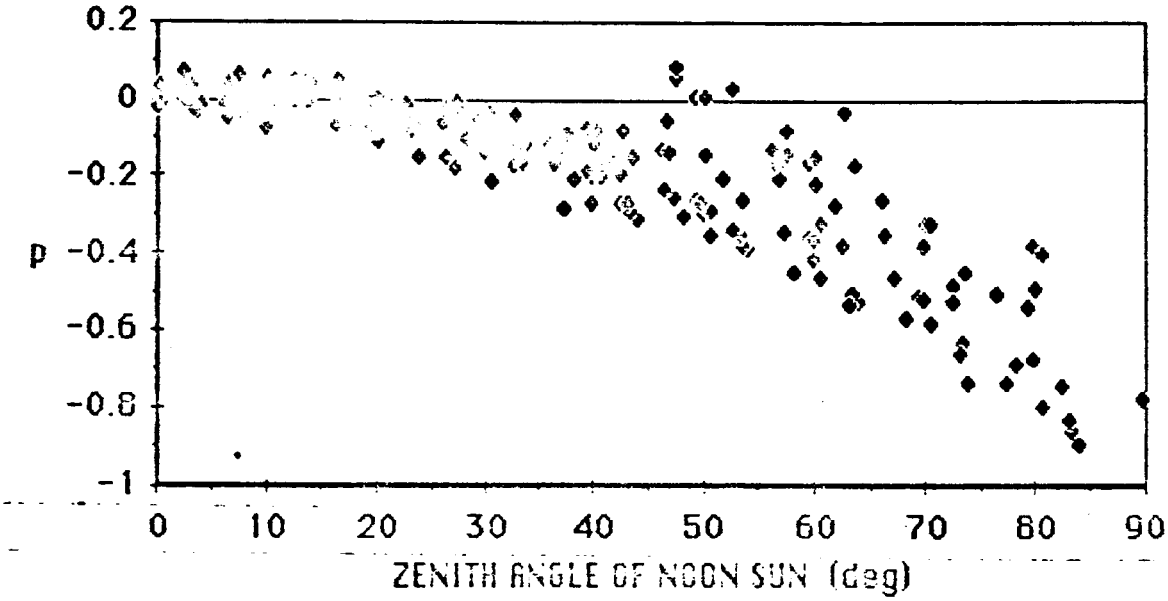

Fig. 17 Scatter plot of all exponent values for the entire year against the zenith angle of the noon sun (defined as the absolute difference between the solar declination and a latitude). These results are based on limb radiances determined from all observation.

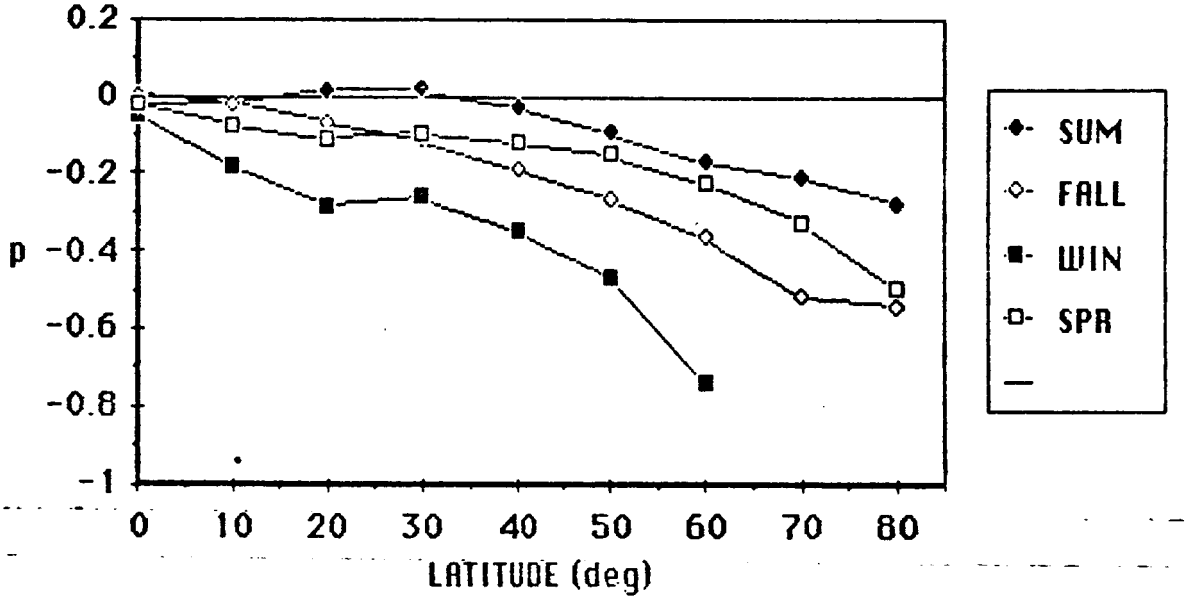

Fig. 18 Seasonal variation of the exponent p with latitude in the NH.

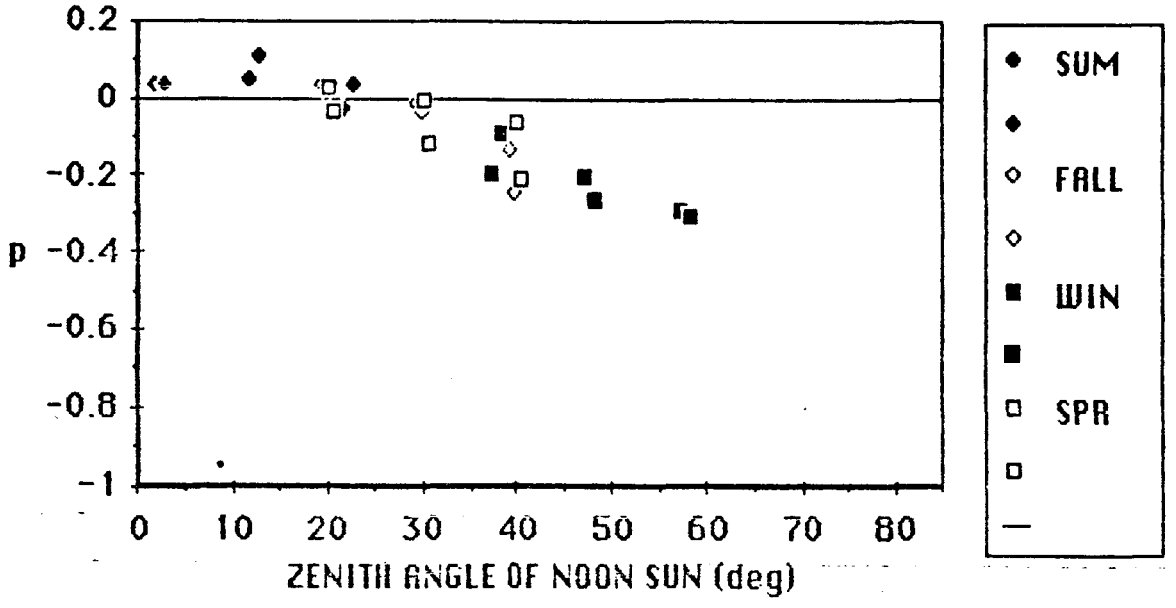

Fig. 19 Seasonal variation of the exponent p for desert regions of the world.

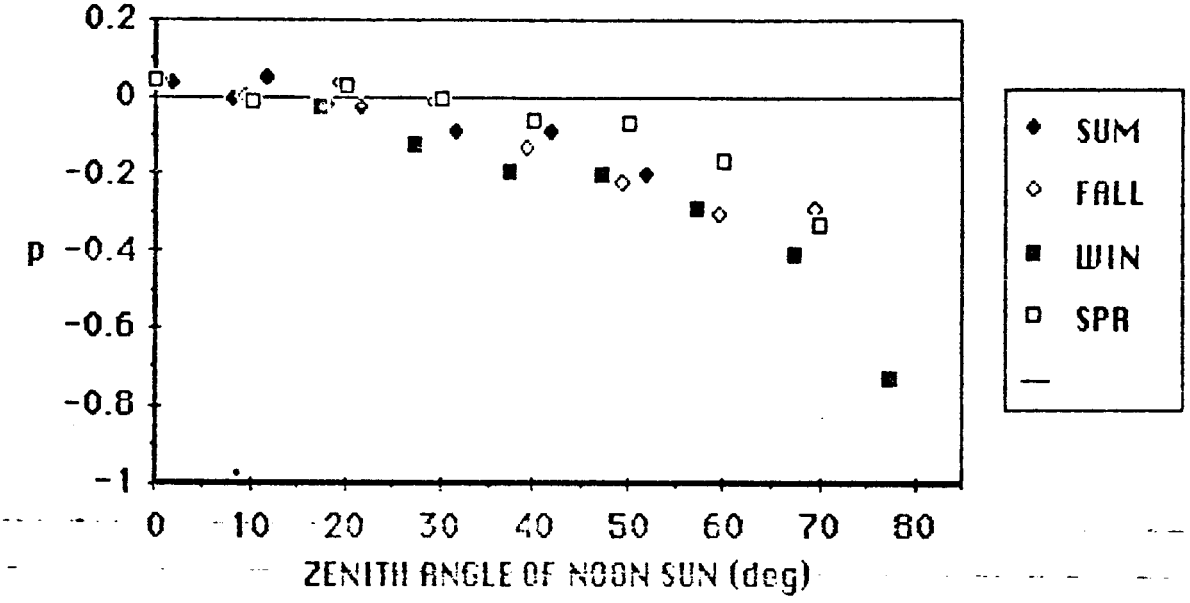

Fig. 20 Seasonal variation of the exponent p for land regions of the NH.

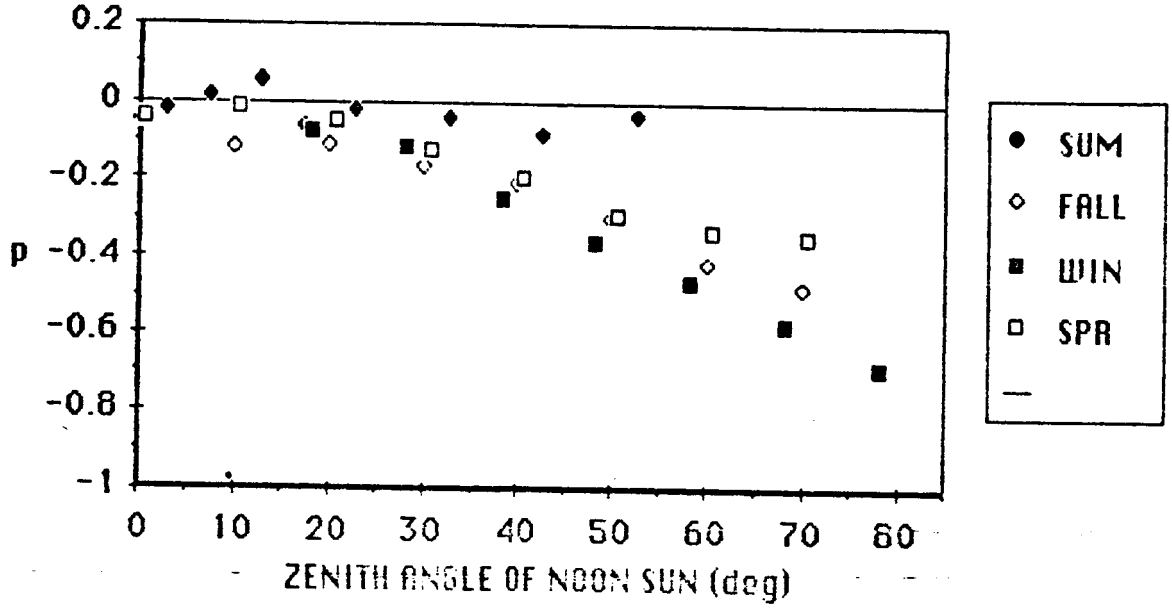

Fig. 21 Seasonal variation of the exponent p for ocean regions of the SH.

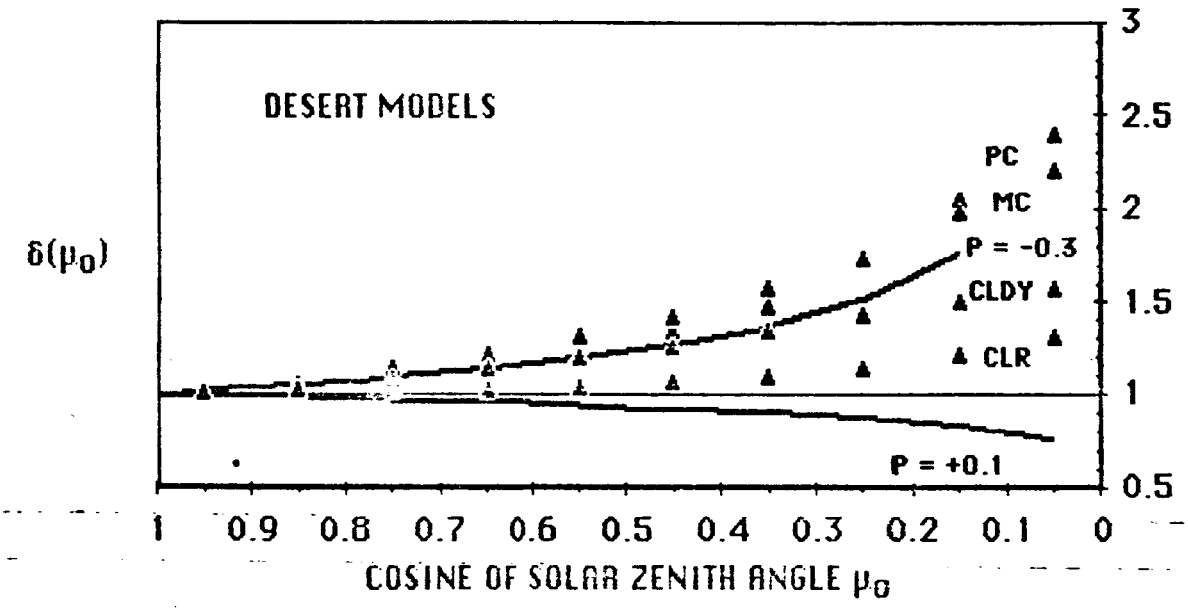

Fig. 22 Comparison of desert models from this study with those employed in the ERBE data processing system (release 3). The curved lines illustrate the range of model variations for exponents shown in Figure 19 of this study. The black triangles illustrate the ERBE models for clear (**CLR**), partly cloudy (**PC**), mostly cloudy (**MC**) and overcast (**CLDY**) desert conditions.

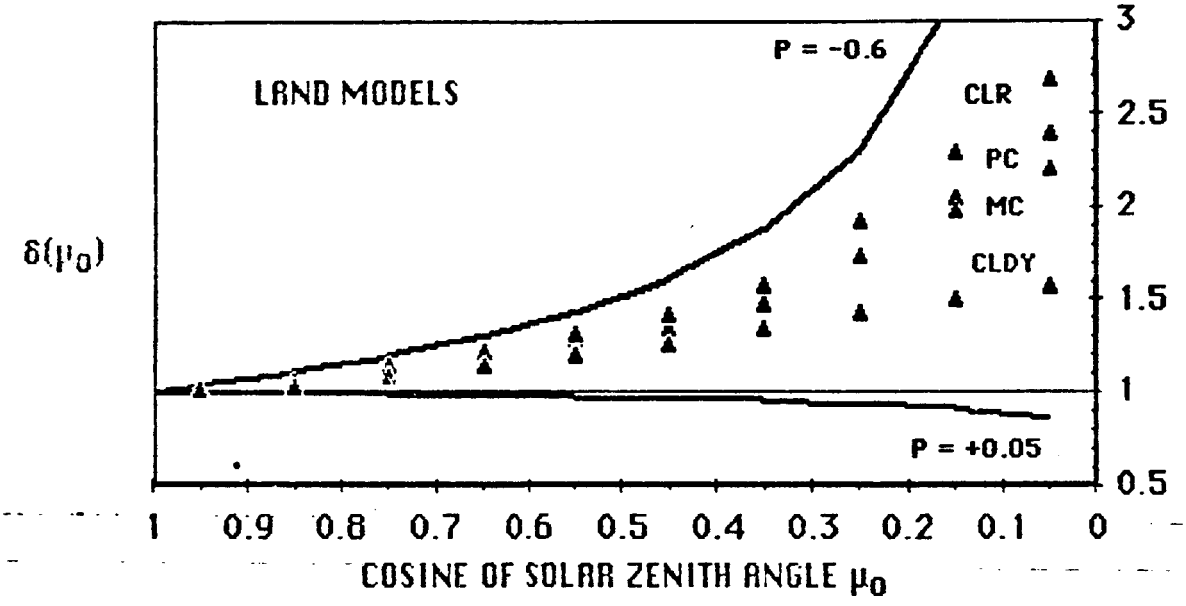

Fig. 23 Comparison of land models from this study with those employed in the ERBE data processing system (release 3). The curved lines illustrate the range of model variations for exponents shown in Figure 20 of this study. The black triangles illustrate the ERBE models for clear (**CLR**), partly cloudy (**PC**), mostly cloudy (**MC**) and overcast (**CLDY**) land conditions.

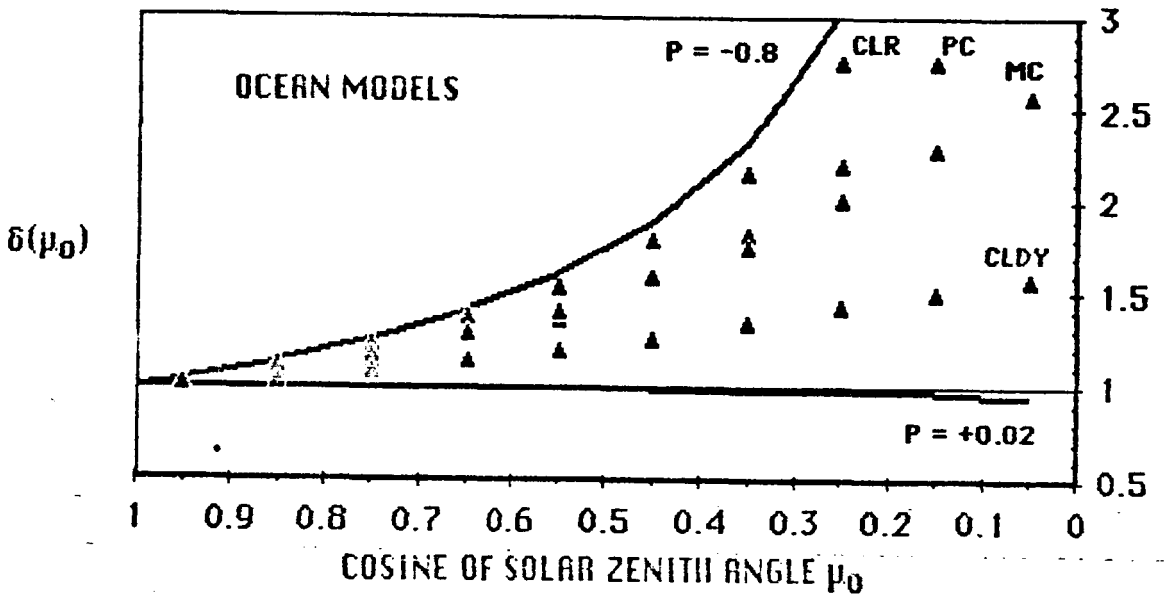

Fig. 24 Comparison of ocean models from this study with those employed in the ERBE data processing system (release 3). The curved lines illustrate the range of model variations for exponents shown in Figure 21 of this study. The black triangles illustrate the ERBE models for clear (**CLR**), partly cloudy (**PC**), mostly cloudy (**MC**) and overcast (**CLDY**) ocean conditions.

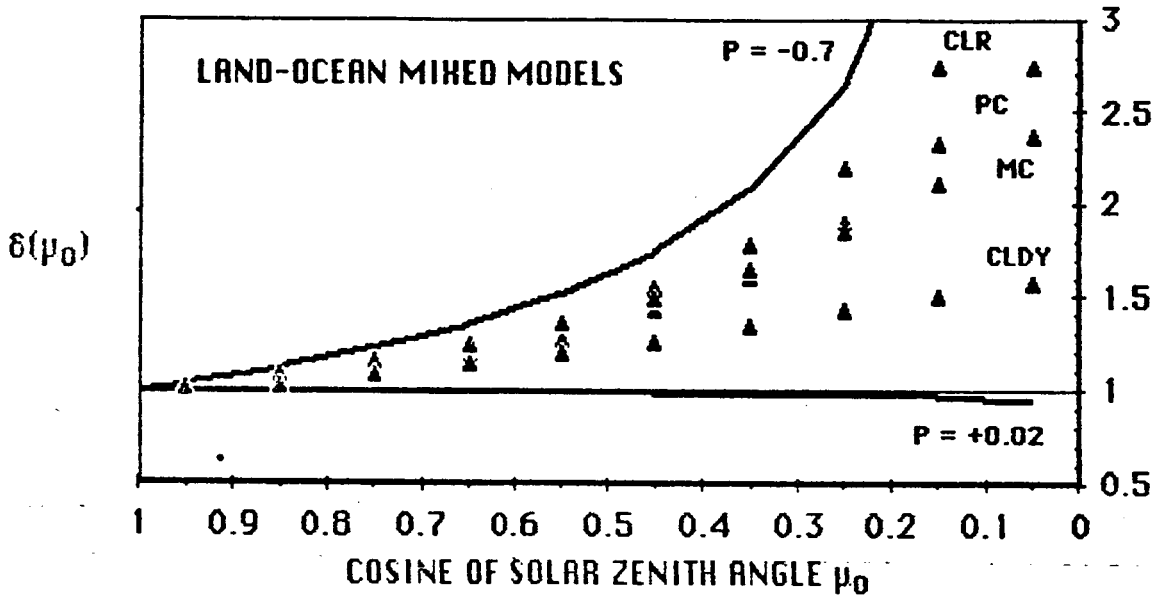

Fig 25 Comparison of land-ocean mixed models from this study with those employed in the ERBE data processing system (release 3). The curved lines illustrate the range of model variations determined in this study. The black triangles illustrate the ERBE models for clear (**CLR**), partly cloudy (**PC**), mostly cloudy (**MC**) and overcast (**CLDY**) land-ocean mixed conditions.

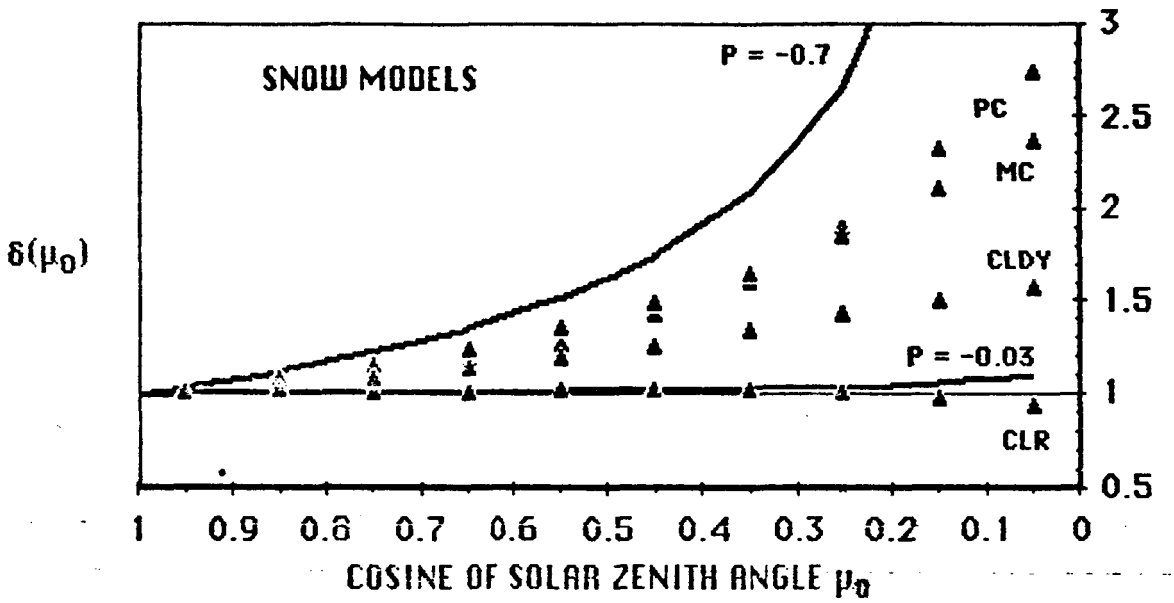

Fig. 26 Comparison of snow models from this study with those employed in the ERBE data processing system (release 3). The curved lines illustrate the range of model variations for exponents determined in this study. The black triangles illustrate the ERBE models for clear (**CLR**), partly cloudy (**PC**), mostly cloudy (**MC**) and overcast (**CLDY**) snow conditions.